Journal of Energy Chemistry 48 (2020) 334–343

Contents lists available at ScienceDirect

Journal of Energy Chemistry

journal homepage: www.elsevier.com/locate/jechem

http://www.journals.elsevier.com/journal-of-energy-chemistry/

Comprehensively-modified polymer electrolyte membranes with multifunctional PMIA for highly-stable all-solid-state lithium-ion batteries

Lehao Liu[a], Jinshan Mo[a], Jingru Li[a], Jinxin Liu[a], Hejin Yan[a], Jing Lyu[b], Bing Jiang[a], Lihua Chu[a], Meicheng Li[a,*]

[a] State Key Laboratory of Alternate Electrical Power System with Renewable Energy Sources, School of Renewable Energy, North China Electric Power University, Beijing 102206, China
[b] Suzhou Institute of Nano-tech and Nano-bionics, Chinese Academy of Sciences, Suzhou 215123, Jiangsu, China

ARTICLE INFO

Article history:
Received 28 December 2019
Revised 23 February 2020
Accepted 23 February 2020
Available online 28 February 2020

Keywords:
Poly(m-phenylene isophthalamide)
Composite polymer electrolyte
Ion conductance
Mechanical strength
Solid-state battery

ABSTRACT

Polyethylene oxide (PEO)-based electrolytes have obvious merits such as strong ability to dissolve salts (e.g., LiTFSI) and high flexibility, but their applications in solid-state batteries is hindered by the low ion conductance and poor mechanical and thermal properties. Herein, poly(m-phenylene isophthalamide) (PMIA) is employed as a multifunctional additive to improve the overall properties of the PEO-based electrolytes. The hydrogen-bond interactions between PMIA and PEO/$TFSI^-$ can effectively prevent the PEO crystallization and meanwhile facilitate the LiTFSI dissociation, and thus greatly improve the ionic conductivity (two times that of the pristine electrolyte at room temperature). With the incorporation of the high-strength PMIA with tough amide-benzene backbones, the PMIA/PEO-LiTFSI composite polymer electrolyte (CPE) membranes also show much higher mechanical strength (2.96 MPa), thermostability (419 °C) and interfacial stability against Li dendrites (468 h at 0.10 mA cm^{-2}) than the pristine electrolyte (0.32 MPa, 364 °C and short circuit after 246 h). Furthermore, the CPE-based $LiFePO_4$/Li cells exhibit superior cycling stability (137 mAh g^{-1} with 93% retention after 100 cycles at 0.5 C) and rate performance (123 mAh g^{-1} at 1.0 C). This work provides a novel and effective CPE structure design strategy to achieve comprehensively-upgraded electrolytes for promising solid-state battery applications.

1. Introduction

The utilization of organic liquid electrolytes in lithium-ion batteries (LIBs) usually results in the safety problems such as leakage, flammability and side reactions [1,2]. The replacement of the organic liquid electrolytes by solid-state-electrolytes (SSEs) is expected to eliminate these safety issues and meanwhile achieve higher energy density by applying Li metal anodes and conversion-typed oxygen/sulfur electrodes [3–5]. The SSEs can also work as separators and thereby offer the possibility of simplifying the battery preparation process [6].

Compared to inorganic SSEs, solid polymer electrolytes (SPEs) comprised of polymer matrices and Li salts have obvious advantages including low density, good film-formation ability, high flexibility and easy fabrication process [2,7–10]. Particularly, polyethylene oxide (PEO) is considered as an important polymer matrix for SPEs, because of its excellent dissociation ability of Li salts, relatively high ion conductance at high temperature and low cost [11–13]. The SPEs also exhibit lower interfacial resistance with the electrodes than the stiff/brittle ceramic electrolytes [14,15]. Li^+ ions can easily transport in the free volume of the polymer matrices through the intra-/inter-polymer chain hopping, however, the high crystallization degree of the polymer matrices and the slow-down dynamics of the polymer chains limit the ionic conductivity (10^{-8}–10^{-6} S cm^{-1}) at room temperature [16–21]. Increasing the operation temperature can elevate the ionic conductivity, but the SPEs lose the dimensional stability being in the molten state [16,22,23]. Besides, the inadequate mechanical strength causes the penetration of the SPEs by Li dendrites especially at high current densities [16,24–26]. Thus, it needs to improve the ion conductance, mechanical strength and thermostability of the SPEs for their practical applications in all-solid-state LIBs.

Constructing co-block/cross-linking polymers and adding organic molecule plasticizers can increase the ion conductivity of the

* Corresponding author.
E-mail address: mcli@ncepu.edu.cn (M. Li).

https://doi.org/10.1016/j.jechem.2020.02.033

SPEs, but this causes other issues such as the incompatibility with electrodes and the mechanical property deterioration [25,27–29]. Fabricating composite polymer electrolytes (CPEs) by adding inorganic nanoparticles (NPs) into the polymer matrices can simultaneously enhance the ionic conductivity, mechanical strength and thermostability [30–33]; however, this method cannot greatly improve the ion conductance and mechanical properties, due to the poor dispersity of the large-surface-area nanofillers [34–38] and the failure to form interconnected reinforcements in the matrices [4,24,39,40], respectively. Besides, the synthesis of these nanofillers is of low efficiency and high cost [11,15,41].

By contrast, polymer blending is regarded as a simple, cheap and scalable method to fabricate high-performance CPEs by integrating PEO/Li salts with polymer molecule additives [11,42–44], and the electrolyte properties can be optimized by combining the advantages of several kinds of polymers [31,45]. A few researchers have reported that the utilization of poly(propylene carbonate) (PPC) [46], poly(4-vinylphenol-co-2-hydroxyethyl methacrylate) (PVPh) [47] and poly(methyl methacrylate) (PMMA) [48] can greatly increase the ionic conductivity of the PEO-based electrolytes by inhibiting the PEO crystallization through the interactions between PEO and the additives, however, they did not investigate the impact of the polymer additives on the mechanical properties. Other researchers even did not compare the ionic conductivity of the CPEs containing poly(methyl hydrosiloxane) (PMHS) [44] and poly(vinyl pyrrolidone) (PVP) [49] additives with that of the additive-free electrolytes. On the other hand, it is reported that the addition of polyurethane (PU) [11,43], PMMA [50], poly (dimethyl siloxane) (PDMS) [51] and poly(vinylidene fluoride-hexafluoropropylene) (PVDF-HFP) [52] can enhance the mechanical strength, but would lower the ionic conductivity. To the best of our knowledge, there are few reports about the comprehensive improvement of the PEO-based electrolyte properties of ionic conductivity, mechanical strength and thermostability by the polymer blending method. Besides, most of these researches have not given the electrochemical properties of the polymer blend electrolyte-based all-solid-state LIBs. So it is necessary to develop novel polymer additives with unique molecule structures or multiple functionalities to enhance the overall properties of the PEO-based SPEs for their practical applications in LIBs.

Similar to poly(p-phenylene terephthalamide) (PPTA), poly(m-phenylene isophthalamide) (PMIA) with meta-type amide-benzene linkages in its skeletal chains has high mechanical strength (3.8 GPa), thermal resistance (400 °C), low electro-conductivity and good chemical stability, and is regarded as an important membrane material [53–55]. Recently aromatic polyamides are employed to prepare various nanocomposite membranes as separators in the conventional liquid electrolyte-based LIBs [55–58]. The polar carbonyl groups in the polyamides can greatly increase the electrolyte wettability of the separators for higher ionic conductivity [55,58]. Moreover, the hydrogen-bond interactions between PEO and the amide groups of the polyamides can effectively reduce the PEO crystallization in the PEO/PPTA nanocomposite [56]. With the incorporation of the high-strength aromatic polyamide components, the nanocomposite membranes also exhibit both greatly-enhanced mechanical strength to suppress the Li dendrite growth [56,57] and thermal stability (up to 240 °C) [58]. Thus, PMIA may be a proper multifunctional additive for fabricating CPE membranes with comprehensively-updated properties such as ionic conductivity, mechanical strength and thermostability.

In this study, novel CPE membranes based on PMIA, PEO and lithium bis(trifluoromethylsulphonyl)imide (LiTFSI) were facilely prepared by the polymer blending technology and subsequent casting process (Fig. 1a). The utilization of the PMIA additive was expected to improve the overall properties of the PEO-based electrolyte, based on these considerations: (1) The hydrogen-bond interactions between the –NH groups in PMIA and –O– groups in PEO can suppress the PEO crystallization and meanwhile reduce the coordination interaction between –O– groups in PEO and Li^+ cations, thus increasing the ionic conductivity of the SPEs (Fig. 1b and c); (2) the hydrogen-bond interactions between the –NH groups in PMIA and $TFSI^-$ anions can facilitate the dissociation of LiTFSI to offer more free Li^+ ions for fast ion transport; (3) apart from the improvement in Li^+ ion conductivity, the incorporation of the high-strength PMIA additive with benzene-amide backbones would greatly enhance the mechanical properties and thermostability.

Various measurements such as Fourier transform infrared spectroscopy, thermogravimetric analysis and electrochemical impedance spectroscopy were further used to investigate the impact of the PMIA additive on the PEO-based electrolyte. It was found that the addition of PMIA greatly enhanced the overall properties such as ion conductance (6.0×10^{-6} S cm^{-1} at ambient temperature), mechanical strength (2.96 MPa), thermodecomposition stability (419 °C), and interfacial stability against Li dendrites (468 h at 0.10 mA cm^{-2}, Tables S1–S3). The PMIA/PEO-LiTFSI CPE-based all-solid-state $LiFePO_4$/Li cells were also assembled and tested. It was demonstrated that the CPE-based cell exhibited better cycling performance (e.g., 137 mAh g^{-1} after 100 cycles at 0.5 C, and 123 mAh g^{-1} at 1.0 C) than the pristine PEO-LiTFSI electrolyte-based cell and other CPE-based cells reported recently (Table S4). Hence, this work offers a novel and effective CPE structure design method to comprehensively upgrade the SPEs for promising all-solid-state battery applications.

2. Experimental

2.1. Fabrication of the electrolyte membranes

PMIA solution was prepared by dissolving PMIA micro-fibers in LiCl/dimethylacetamide (DMAc) solution (Fig. S1) [59]. Specifically, 3.00 g PMIA fibers and 0.30 g LiCl were put in 30 mL DMAc and then stirred vigorously at 60 °C for 6 h until the complete dissolution of PMIA and the formation of semitransparent PMIA/DMAc solution (Fig. S2). PEO-LiTFSI electrolyte membrane was fabricated by dissolving 0.66 g LiTFSI and 1.83 g PEO (molecule weight: 600,000) in 50 mL DMAc at 60 °C for 4 h, putting the LiTFSI/PEO/DMAc mixture solution in a Teflon plate, and then drying in vacuum condition at 60 °C for 48 h. The CPE membranes with different weight ratios of PMIA were fabricated by adding the abovementioned PMIA/DMAc solution, 1.83 g PEO, and LiTFSI (with the EO/Li ratio of 18) in DMAc (50 mL in total) followed by the stirring, casting and drying processes. The contents of the electrolyte components were given in Table S5. The CPEs with 0, 1 wt%, 5 wt%, 10 wt% and 20 wt% PMIA were denoted as PMIA0, PMIA1, PMIA5, PMIA10 and PMIA20, respectively. Similarly, the PMIA-LiCl-LiTFSI electrolyte with 0.92 g PMIA was also obtained by adding moderate LiTFSI in the PMIA/DMAc solution, and this electrolyte was labeled as PMIA-LiTFSI for convenience. All the electrolyte membranes were put in a glove box filled with argon for at least three days before various characterizations.

2.2. Materials characterizations

The micro-morphology of the electrolytes was determined by a FEI Quanta 200F or Hitachi SU8010 scanning electron microscope (SEM) coupled with energy dispersive X-ray spectroscopy (EDS). The applied voltages for taking SEM and EDS images were 3.0 and 20.0 kV, respectively. The crystal structure was detected by a Bruker D8 Focus X-ray diffraction (XRD) analyzer (Cu K_α radiation, λ=0.154 nm). The thermostability was measured by a

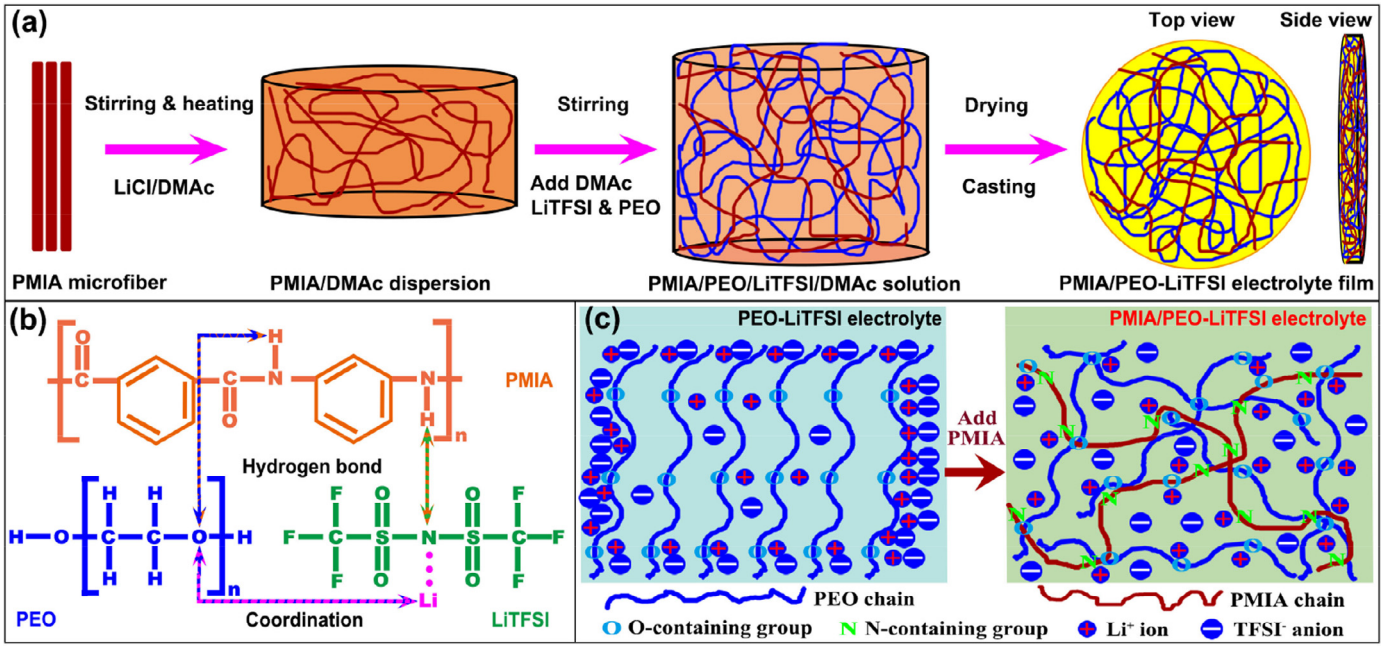

Fig. 1. (a) Schematic description of the fabrication process of PMIA/PEO-LiTFSI CPE membranes. (b) Interactions between PMIA, PEO and LiTFSI. (c) Structure of the PEO-LiTFSI electrolyte before and after the incorporation of PMIA.

D840TA Q500 thermo-gravimetric analyzer (TGA) under a heating speed of 10 °C min^{-1}. The mechanical tensile properties were tested by a GOTECH AI-7000-ST mechanical tester under a speed of 2 mm min^{-1}. The Fourier transform infrared (FTIR) absorbance spectra were obtained using a PerkinElmer Frontier FTIR spectroscopy analyzer. Differential scanning calorimetry (DSC) measurements were conducted using a TA Q2000 instrument in N_2 flow. The electrolyte samples (~20 mg) were cooled down from room temperature to −90 °C at 5 °C min^{-1}, kept at −90 °C for 10 min, and then heated to 110 °C for recording the data. The percentage of crystalline PEO (X_c) was calculated from the classic equation: $X_c = (\Delta H/\Delta H^o f) \times 100\%$, where ΔH and ΔH^o represented the fusion heat of the electrolytes (the integral area of the DSC curves) and the melting enthalpy of the completely-crystallized PEO (213.7 J g^{-1} for 100% crystalline), respectively, and f was the PEO weight ratio in the electrolytes [47,60].

2.3. Electrochemical measurements

Different cells of stainless steel (SS)/SPE/SS, Li/SPE/Li, SS/SPE/Li and $LiFePO_4$/SPE/Li were fabricated in argon condition for various electrochemical measurements. The $LiFePO_4$ electrodes with ~2.0 mg cm^{-2} mass loading were obtained by coating a mixture slurry of poly(vinylidene fluoride) (PVDF), $LiFePO_4$, carbon nanotube and carbon black (1:8:0.03:0.97, wt/wt) on Al foils, and then drying at 60 °C for 24 h in vacuum condition. To obtain the ionic conductivity of the SPEs, the electrochemical impedance spectra (EIS) of the SS/SPE/SS cells were acquired in a Zahner Zennium electrochemical workstation within 10^6–10^{-2} Hz at the amplitude of 10 mV. The ion conductivity (σ) was calculated using an equation: $\sigma = L/SR$, where R, S and L were the resistance, surficial area and thickness of the electrolyte membranes, respectively [9,61]. The measurement temperature increased from 30 to 80 °C at 10 °C h^{-1}, and the cells were kept at each measurement temperature for 1.0 h for thermal equilibrium prior to the EIS measurements. The measurements of EIS and chronoamperometry (CA) of the Li/electrolyte/Li cells at 80 °C were conducted to acquire the Li^+ ion transference number (t_{Li+}) of the electrolytes using a classic equation: $t_{Li+} = I^s(\Delta V - I^o R_i^o)/I^o(\Delta V - I^s R_i^s)$, where I^o and I^s are the currents at the initial and steady states, respectively, ΔV is the applied DC polarization potential of 10 mV, and R_i^o and R_i^s are the electrolyte/Li metal interfacial resistances at the initial and steady states, respectively [11,62]. A CHI660E electrochemical workstation was utilized to conduct the linear sweep voltammetry (LSV) measurements with a scanning rate of 1 mV s^{-1}. A Land LANHE CT2001A multichannel battery tester was used to perform the galvanostatic charge-discharge tests with a voltage cutoff of 2.5 − 3.8 V (Li/Li^+) under different C rates (1 C = 170 mA g^{-1}).

3. Results and discussion

3.1. Microstructure

The commercial PMIA purchased from Yantai Tayho (China) was in fiber form with an average length of 6 mm (Fig. S2A–C). To fabricate the composite electrolytes, the PMIA micro-fibers (~10 μm in diameter) were first dissolved in a LiCl/DMAc solution, according to the previous study [59]. The dissolution mechanism of the PMIA fibers is shown in Fig. S1. The $[Li{\bullet\bullet\bullet}DMAc]^+$ macro-cation complexes form between the −C=O groups in DMAc and the Li^+ ions in LiCl, while the Cl^- ions are left unencumbered (Fig. S1A). The active Cl^- ions would break the intra/inter-hydrogen-bonds between the −NH and the −C=O groups in PMIA chains, and then form new interactions with the hydrogen groups on the −NH groups in PMIA chains (Fig. S1B) [59]. Thus, the meta-aramid fibers were completely dissolved in the mixture solution, and a semi-transparent PMIA solution was prepared (Fig. S2D) as additive to attain the PMIA/PEO-LiTFSI CPE membranes.

SEM characterizations were conducted to observe the surficial and cross-sectional microstructures of the electrolytes (Figs. 2 and S3). A lot of wrinkles formed on the surface of the pristine PEO-LiTFSI (PMIA0) electrolyte (Fig. 2a and c), and a few large micro-cracks also generated in the cross-section (Fig. 2b and c) during the sample preparation process for SEM characterizations. The EDS mappings verified the incorporation of the PMIA additive in the PEO-LiTFSI electrolyte by the polymer blending method (Fig. S4). After the incorporation of 1 wt%–5 wt% PMIA additive, less wrinkles generated and the CPE surface became smoother

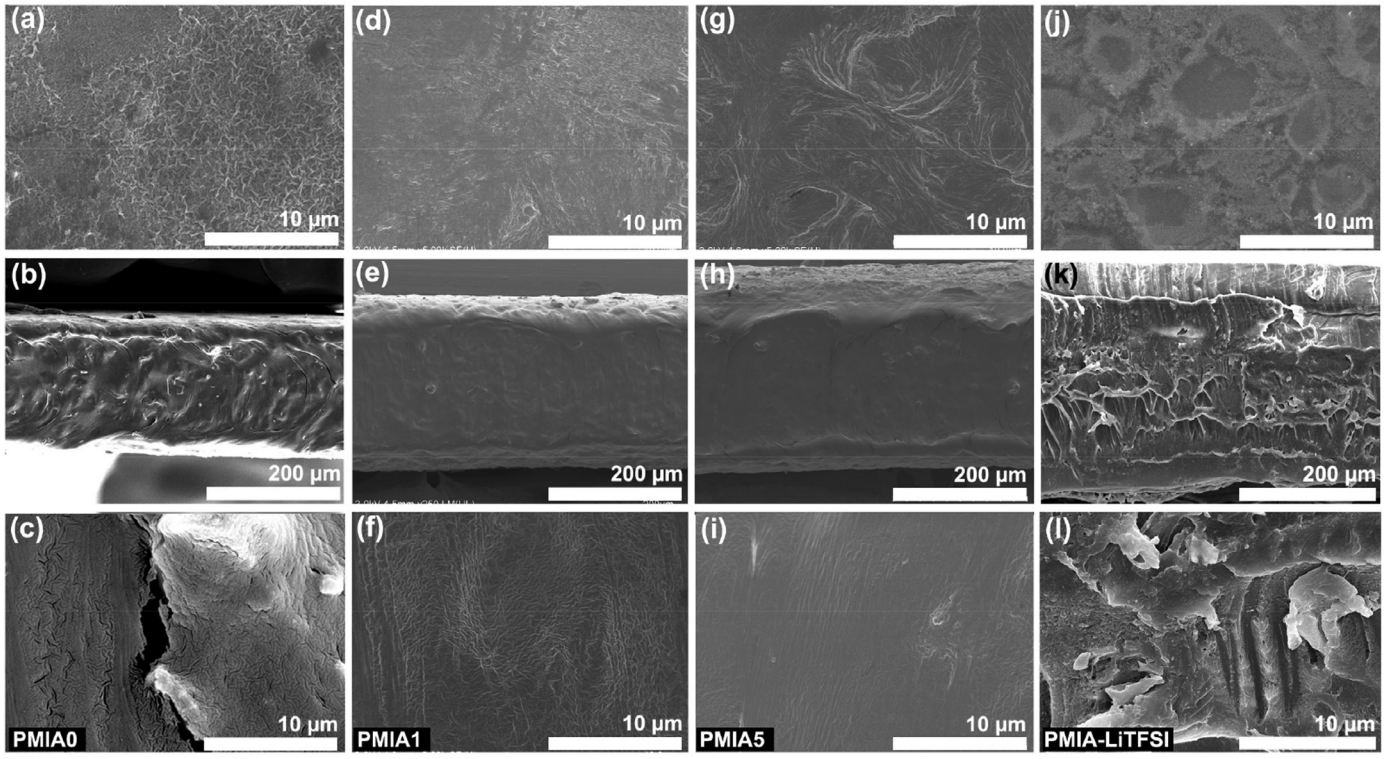

Fig. 2. (a, d, g and j) Surficial and (b and c, e and f, h and i, k and l) cross-sectional SEM images of the composite electrolyte membranes of (a–c) PMIA0, (d–f) PMIA1, (g–i) PMIA5, and (j–l) PMIA-LiTFSI, respectively.

(Fig. 2d–f and g–i), which may be attributed to the reduction of the electrolyte crystallization [63–65]. The crystallization characteristics will be furtherly discussed by XRD and DSC measurements in Section 3.2. However, the excessive addition of PMIA (10 wt%) resulted in the formation of wrinkles and the increase of the surficial roughness (Fig. S3A–C). Compared to the pristine PMIA0 electrolyte, no obvious crack was found in the cross-sections of the PMIA-containing electrolytes (Fig. 2e and f, h and i and S3B and C), which may be ascribed to the enhanced mechanical strength by the PMIA molecule additive (detailed mechanical properties in Section 3.3). We can also clearly see the inhomogeneity of the PMIA-LiTFSI electrolyte (Fig. 2j) and nanosized pores inside the electrolyte (Fig. 2k and l), reflecting the much agglomeration of PMIA and ineffective dissolution of the Li salts. Moreover, the pristine PMIA0 electrolyte film had a thickness of around 196 μm (Fig. 2b), and the film thickness increased to around 264 and 290 μm for the PMIA1 and PMIA5 electrolytes (Fig. 2e and h), respectively, because of the incorporation of the PMIA additive in the pristine electrolyte. This can be verified by the larger thickness of the PMIA-LiTFSI film (around 347 μm for 0.92 g PMIA, Fig. 2k). The changes of the electrolyte microstructures would affect the properties such as ionic conductivity and mechanical stability.

3.2. Ion conductance

The ionic conductivity (σ) can be described using the classic equation:

$$\sigma = \sum C_i Q_i \mu_i \quad (1)$$

where Q_i, C_i and μ_i represent the ion charge, and the concentration and mobility of the charge carriers, respectively [66–68]. In typical polymer electrolyte systems, the dominated ion motions occur in the amorphous polymer regions through the local segmental chain motions (as the driving force for the ion transport), affecting the ion mobility [10,66,67,69,70]. The interactions between the components in the polymer electrolytes also affect the ion concentration. As we know, the elements of Li, H, S, N, Cl, O and F have the electronegativity values of 0.98, 2.18, 2.58, 3.04, 3.16, 3.44 and 3.98, respectively. There is an ion-dipole or coordination interaction between the −O− groups in PEO and the Li^+ ions in LiTFSI [66,68]. The hydrogen-bond interactions between the −NH groups in polyamides (e.g., PPTA, a para-aramid) and the −O− groups in PEO can afford their layer-by-layer assembly for composite membranes [71,72], and there is also hydrogen-bonding between the −NH groups and the −C=O groups [73]. Furthermore, the previous study has proven the strong hydrogen-bond interactions between the −NH groups in PMIA and the Cl^- anions in LiCl, which can break the intra/inter-hydrogen-bonds between the −NH and the −C=O groups in PMIA chains (Fig. S1) [65]. Lu et al. also verified the existence of the strong hydrogen-bond interactions between the –OH groups in celluloses and the Cl^- anions in LiCl [74]. A few studies furtherly find that urea calis [4] arene [75,76] and calix[2]-p-benzo[4]pyrroles [77] can effectively trap the anions (e.g., ClO_4^- and FSI^-) of Li salts by hydrogen-bond interactions through their −NH groups, and thus release more free Li^+ ions in the polymer electrolytes. Thus, the −NH groups in PMIA should have hydrogen-bond interactions with the −O− groups in PEO and the $TFSI^-$ anions in LiTFSI in theory (Fig. 1b), and then have great influence on the electrolytes such as C_i and μ_i.

The hydrogen-bond interactions between PMIA and PEO/LiTFSI matrices were then disclosed by analyzing the change of the FTIR spectra (Fig. 3a and b). Compared to the PMIA-LiTFSI electrolyte, the N–H bending-resulted absorbance peak intensity at around 1544 cm^{-1} increased and became sharp in the PMIA-containing CPE. This indicated that the intra-/inter-hydrogen bonding strength between the PMIA chains decreased after the incorporation of PEO [65], and also suggested the existence of the hydrogen-bond interaction between PMIA and PEO, which led to the surficial struc-

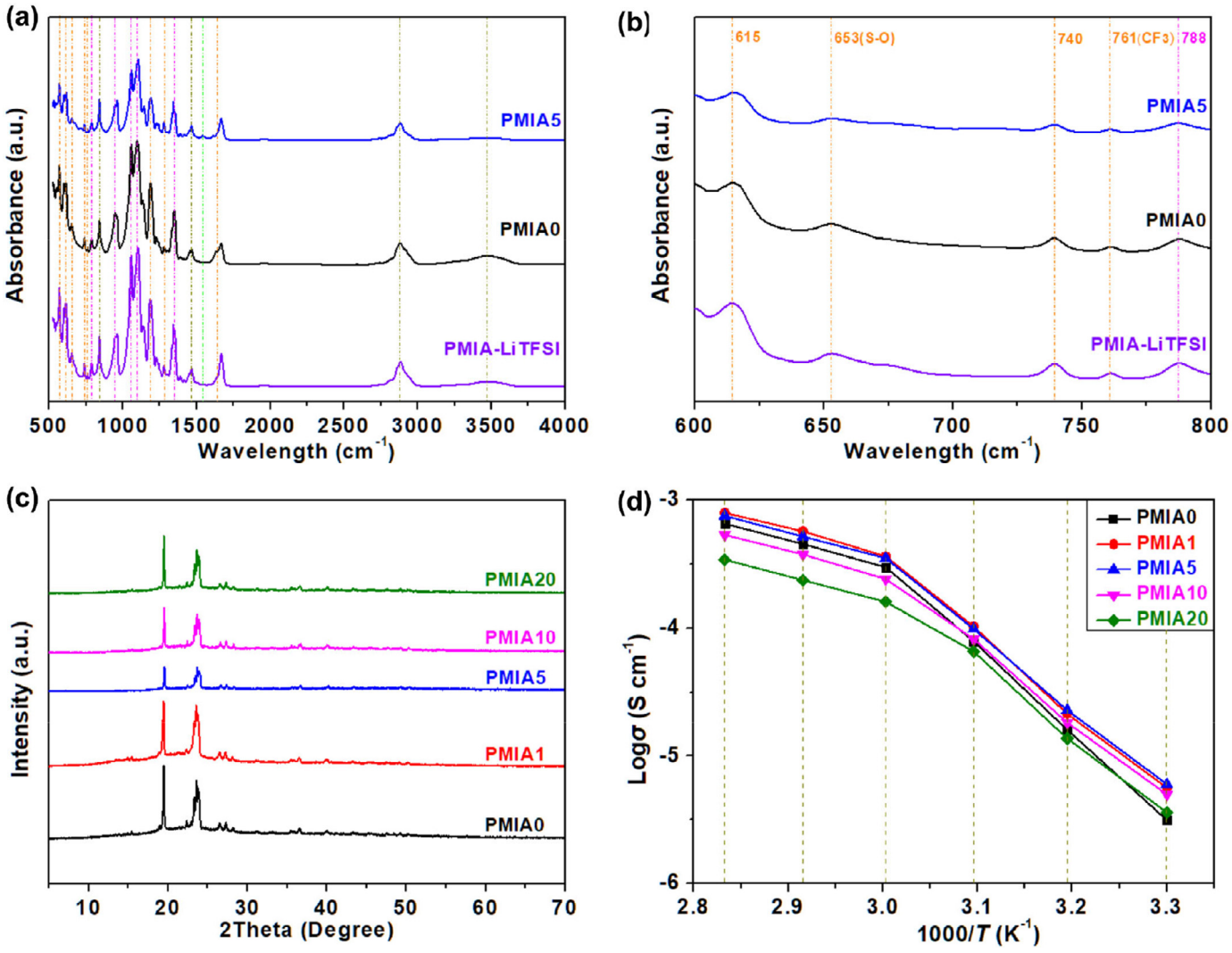

Fig. 3. (a, b) FTIR spectra, (c) XRD patterns, and (d) ionic conductivities of the electrolyte membranes.

ture change of the electrolyte membranes (Fig. 2a–i). Compared to the pristine PEO-LiTFSI electrolyte, the shape and position of the C–O stretching/bending-resulted peaks at around 947, 1094 and 1351 cm^{-1} [28,78] also changed greatly in the CPE, which together manifested the hydrogen-bonding between the N–H groups in PMIA and C–O groups in PEO. This interaction between PMIA and PEO would suppress the crystallization of PEO by perturbing the ordering of the PEO chains. The intensity of a few typical peaks at around 19.5, 23.7 and 36.8° related to the PEO crystallinity [36] decreased in the CPEs with ≤5 wt% PMIA (Fig. 3c), verifying the effective suppression of the PEO crystallization by PMIA. DSC measurements (Fig. S5) showed that the glass transition temperature and melting point of the electrolytes decreased with the addition of PMIA, and the PEO crystallinity in the PMIA5 electrolyte was 46.2%, much lower than that in the pristine PEO-LiTFSI electrolyte (54.8%). The lowering of the PEO crystallization would accelerate the local segmental motions in the amorphous regions, and therefore increase the Li^+ ion mobility (μ_i) by hopping between/along the PEO chains [21,66]. However, high-content PMIA (≥10 wt%) was detrimental to the inhibition of the PEO crystallization (Fig. 3c), because of the increasing hydrogen-bond interaction between the PMIA chains and the induced PMIA agglomeration, which also caused the inhomogeneity and roughness of the electrolyte structure (Fig. S3).

In the electrolytes, a few typical absorbance peaks at around 572, 740, 761 and 1286 cm^{-1} regarding the stretching vibrations of CF_3 and C–F groups in LiTFSI appeared [79,80]. Other characteristic peaks related to S–O stretching, C–SO_2–N stretching and LiTFSI aggregation also appeared at around 653, 1189 and 1631 cm^{-1}, respectively [79,80]. We can see that the PMIA-containing CPE displayed lower peak intensity at 740 and 761 cm^{-1} than the PMIA0 and PMIA-LiTFSI electrolytes (Fig. 3b), indicating that less triflate-containing anions were in pairs in the CPE [80]. The peak intensity at around 1631 cm^{-1} related to the LiTFSI aggregation [79] also decreased greatly in the CPE. Based on these FTIR analyses, the elemental electronegativity values and the previous reports [65,74–77], we can infer that the hydrogen-bond interactions between the –NH groups in PMIA and the $TFSI^-$ anions (mainly the F atoms, due to the high F electronegativity and the F-related peak intensity change) led to the effective dissociation and dissolution of LiTFSI. These results were consistent with the SEM analyses (Fig. 2). The dissociation of LiTFSI would increase the free Li^+ ion concentration (C_i) and thus facilitate the ion conduction in the CPEs. The PMIA5 composite electrolyte showed much higher Li^+ ion transference number (t_{Li+}) of 0.52 than the pristine PEO-LiTFSI electrolyte with a t_{Li+} of 0.29 (Fig. S6), consistent with the previous reports of 0.2–0.3 [11,62,81]. This furtherly manifests the effective immobilization ability of $TFSI^-$ anions by the multifunctional

PMIA additive, in accordance with the FTIR analyses (Fig. 3a and b). The high t_{Li+} would also reduce the ion concentration gradient in the PMIA5 electrolyte, inhibit the undesirable side reactions on the electrodes, and improve the electrochemical performance of the CPE-based cells [20,82].

According to the classic ionic conductivity Eq. (1), either increase of C_i or μ_i can increase the ion conductivity (σ) of the polymer electrolyte. Based on the abovementioned theoretical and experimental analyses, we can easily conclude: (1) the hydrogen-bonding between PMIA and PEO can inhibit the PEO crystallization, accelerate the PEO chain motions, and thus increase the Li^+ ion mobility (μ_i); (2) the hydrogen-bonding between PMIA and $TFSI^-$ in LiTFSI can promote the dissolution and dissociation of LiTFSI in the PEO matrices, and therefore increase the concentration of the free Li^+ cations (C_i) in the electrolytes; (3) the hydrogen-bonding between PMIA and PEO would weaken the coordination strength between the –O– groups in PEO and the Li^+ cations [66], and increase the free Li^+ cation concentration (C_i). Because of these synergistic effects, the CPE membrane with 5 wt% PMIA showed a greatly-improved ambient temperature ionic conductivity of 6.0×10^{-6} S cm^{-1}, which was two times that (3.1×10^{-6} S cm^{-1}) of the pristine PEO-LiTFSI electrolyte (Figs. S7 and 3d, and Table S1). In distinct comparison, the incorporation of other polymer additives such as PU [11,43] and PDMS [51] resulted in the decrease in the ionic conductivity, possibly ascribed to the poor interactions between the electrolyte matrices and the additives. The 1 wt% PMIA-containing CPE showed much higher ionic conductivities ($\geq 3.6 \times 10^{-4}$ S cm^{-1}) at $\geq$60 °C, owing to the increased chain mobility at higher temperatures and the low content of the stiff PMIA additive with poor ion conduction property. Moreover, the CPEs with high-content PMIA of $\geq$10 wt% showed lower ionic conductivities at high temperatures of $\geq$60 °C, owing to the inhomogeneity of the electrolyte composition (Fig. S3) and also the insufficient ion transfer property of the stiff PMIA additive.

The relationship between the ion conductance and the temperature follows the Arrhenius equation:

$$\sigma = Aexp(-E_a/RT) \quad (2)$$

where *A, R, T, and* E_a, represent the pre-exponential factor, gas constant (8.314 J $mol^{-1}k^{-1}$), absolute temperature, and activation energy, respectively [27]. In the low temperature range of 30–60 °C, the CPE with 5 wt% PMIA showed lower activation energy of 110 kJ mol^{-1} than the pristine PEO-LiTFSI electrolyte (128 kJ mol^{-1}), indicating the lower energy barrier and faster ion transport in the PMIA-modified CPE [83]. However, all the electrolytes had the similar and lower activation energy of around 38 kJ mol^{-1} in the temperature range of 60–80 °C, because of the great increase of the ion mobility and the polymer chains at high temperatures [69,70].

3.3. Mechanical, electrochemical and thermal properties

Apart from ionic conductance, mechanical, electrochemical and thermal stabilities were also important to the practical applications of the SPEs in Li-ion batteries especially operated at high temperatures. The mechanical tensile stress-strain curves were shown in Fig. 4(a). The pristine PMIA0 electrolyte membrane had an ultimate tensile strength of 0.32 MPa. In sharp contrast, the PMIA-LiTFSI electrolyte showed a much higher ultimate tensile stress of 10.51 MPa. The PMIA-containing CPE membrane with 5 wt% PMIA also exhibited a decent ultimate tensile stress of 2.96 MPa, which was attributed to the reinforcement effect of the high-strength PMIA with tough amide-benzene backbones and the formed continuous PMIA chain networks. The mechanical tensile strength of the PMIA5 electrolyte was also higher than those of the PEO-based composite electrolytes modified with $Li_{10}SnP_2S_{12}$ particle (0.8 MPa) [84], aluminosilicate nanoparticle (1.0 MPa) [32], vermiculite nanosheet (0.8 MPa) [81], g-C_3N_4 nanoplate (0.4 MPa) [15] and $Mg_2B_2O_5$ nanowire (2.3 MPa) [33], and comparable to that of the 3D polyimide-PEO framework-based electrolyte (3.3 MPa) [85]. Due to the incorporation of the high-modulus PMIA (168.73 MPa), the 5 wt% PMIA/PEO-LiTFSI CPE film also showed a Young's modulus of 37.07 MPa, which was ~38 times higher than the pristine one (0.98 MPa). According to the LSV measurement at 60 °C (Fig. S8), the CPE membrane with 5 wt% PMIA displayed a high oxidation potential of around 4.4 V vs. Li/Li^+, which could meet the requirement of most of the Li-ion battery applications [55].

TGA measurements were performed to detect the thermostability of the electrolyte membranes (Fig. 4b). The PMIA5 electrolyte had an extra 4 wt% loss before 200 °C compared to the pristine electrolyte, which may be ascribed to the decomposition of the polyamide (Fig. S9) [86]. However, the PMIA5 CPE showed higher main thermal decomposition temperature of 419 °C than the pristine PMIA0 electrolyte (364 °C), due to the incorporation of the high-thermostability PMIA additive. The thermostability of the electrolyte membranes was then determined by observing the shape change of the membranes at 160 °C in ambient atmosphere (Fig. 4c–f). The CPE membranes with low-content PMIA (0 and 1 wt%) easily melted after 0.5 h (Fig. 4c). Nevertheless, high-content PMIA-containing CPE membranes (5 wt%, 10 wt% and 20 wt%) still remained their original shape even after 10.0 h (Fig. 4f), again proving the high thermostability of the PMIA-based CPEs. The great improvement in the mechanical strength and thermal stability would effectively delay the Li dendrite nucleation in the CPEs and meanwhile prevent the crack growth in the electrolytes by the Li dendrite penetration [81].

3.4. Interfacial resistance against Li dendrites

Galvanostatic cycling was conducted to test the durability of the electrolyte membranes at 0.10 mA cm^{-2} and 60 °C with the change of the current direction every 300 s in the Li/SPE/Li symmetric cell configuration (Fig. 5a–d). Li^+ ions were alternatively stripping/plating during the periodic charging/discharging processes and may lead to the formation/growth of Li dendrites. The PMIA0 electrolyte-based cell showed an original overpotential of around 0.02 V, but the overpotential suddenly dropped to 0 V after 246 h (Fig. 5a), suggesting the penetration of the electrolyte membrane by the Li dendrites [87,88]. In comparison, no short circuit occurred in the PMIA-containing cells (Fig. 5b–d). Moreover, the PMIA5 and PMIA10 electrolyte-based cells almost kept the original potentials during the whole cycling (Fig. 5c and d). Specifically, the overpotential of the PMIA5 electrolyte-based cell remained at around 0.013 V for 468 h (Fig. 5c), because of the greatly-improved mechanical strength against Li dendrites and ionic conductance. The cycling performance of the symmetric cells at higher current densities and charge/discharge times was further studied. When cycled at 0.30 mA cm^{-2} and 60 °C with the charge or discharge time of 1 h (i.e., areal capacity of 0.30 mAh cm^{-2} comparable to that of commercial LIBs, Fig. S10A–C), or at 0.10 mA cm^{-2} and 40 °C with the charge or discharge time of 1 h (i.e., areal capacity of 0.10 mAh cm^{-2}, Fig. S10D–F), the PMIA-based cells still maintained the relatively stable potentials, but the PMIA-free cells had much shorter cycling lifetimes (around 90 and 174 h).

EIS measurements were then applied to investigate the impedance change of the cells during the galvanostatic cycling (Fig. 5e and f and Table S2). The circles at the high and low frequencies were related to the ohmic resistance from the electrolytes (R_e) and the interfacial resistance (R_i) between the electrolytes and the Li metal electrodes, respectively [3,36,87,89,90]. The total resistance (R_t) of the PMIA0 electrolyte-based cell decreased from

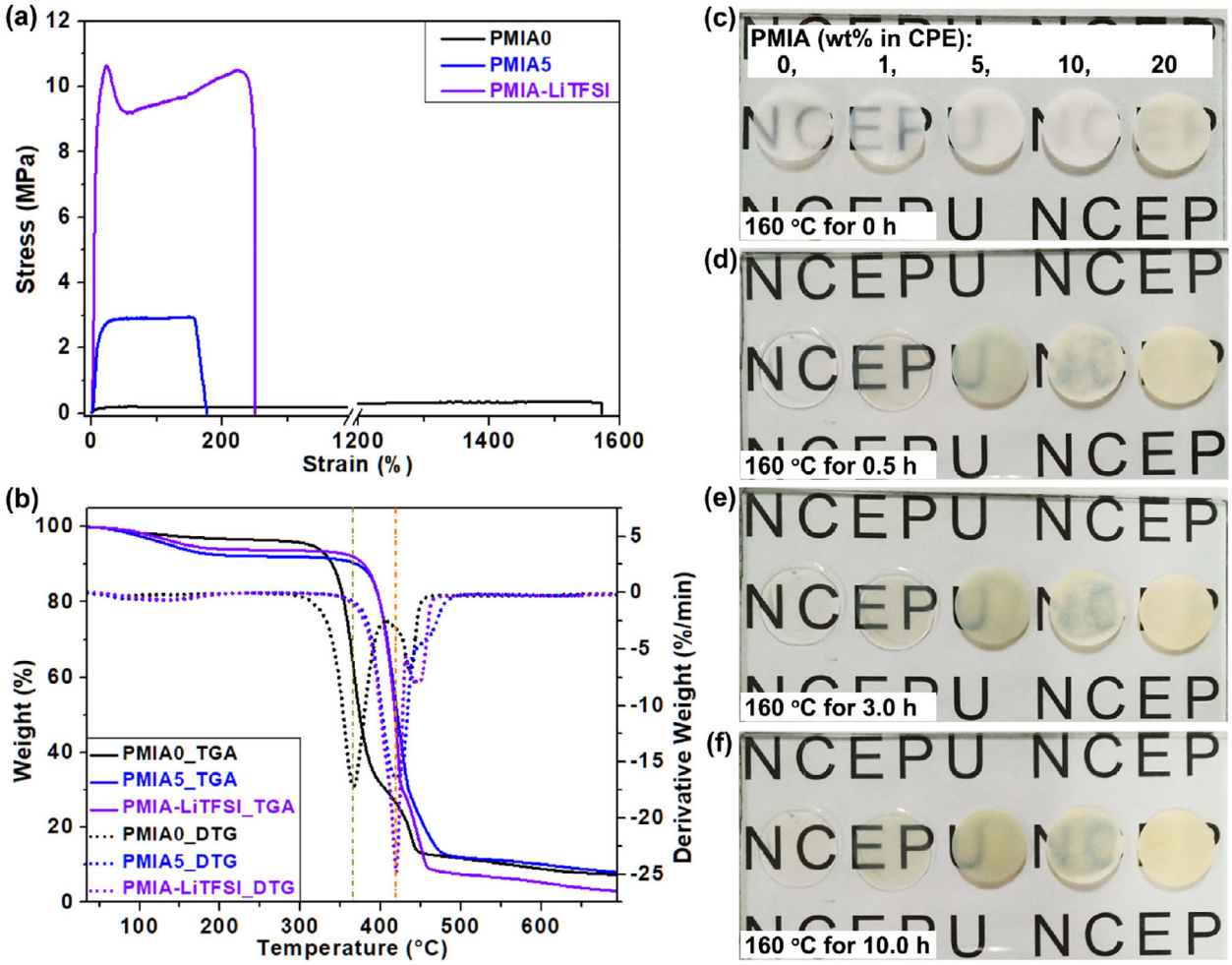

Fig. 4. (a) Mechanical tensile stress-strain curves, (b) TGA curves, and optical photographs of the electrolyte membranes at 160 °C for (c) 0, (d) 0.5, (e) 3.0 and (f) 10.0 h.

around 138 to 3 ohm after the galvanostatic cycling, suggesting the short circuit of the cell by the Li dendrite penetration, consistent with the potential profile in Fig. 5(a). The PMIA0-based cell did not show a total resistance of 0 ohm after the short circuit, which should be ascribed to the formation of passivation layers [91] and the nonzero resistance of the Li dendrites [92]. In contrast, the PMIA-based cells showed increasing total resistances during the whole cycling (i.e., from 122, 78 and 166 to 139, 100 and 221 ohm for the electrolytes with 1 wt%, 5 wt% and 10 wt% PMIA, respectively), again proving the higher interfacial stability of the PMIA-containing electrolyte membranes during the Li stripping/plating processes. The interfacial resistances also increased from 82, 43 and 86 ohm to 129, 94 and 183 ohm for the PMIA1, PMIA5 and PMIA10 electrolyte-based cells, respectively, owing to the formation of the passivation layers [91]. Among these PMIA-containing cells, the PMIA5-based cell exhibited the lowest R_e, R_i and R_t values before and after the Li stripping/plating processes.

SEM images were further taken to detect the surficial microstructure change of the electrolyte membranes after the galvanostatic cycling (Figs. 5g–l and S11). We can clearly see large protrusions on the PMIA0 electrolyte surface along with the microcracks (Fig. 5g and h), which should be the reason of the short circuit of the Li/SPE/Li cell during the Li stripping/plating processes (Fig. 5a). Similarly, a lot of Li deposition-resulted microparticles also formed on the PMIA1 electrolyte surface (Fig. 5i and j). However, there was almost no protrusion on the surfaces of the PMIA5 and PMIA10 electrolytes (Figs. 5k and l and S11). These SEM results together with the EIS and galvanostatic cycling analyses verified the higher interfacial resistance of the PMIA-containing CPE membranes against Li dendrites than the PMIA-free electrolyte membrane, and also agreed with the aforesaid discussion that the greatly-enhanced mechanical strength and thermostability of the PMIA-modified electrolytes can effectively suppress the nucleation and growth of the Li dendrites.

3.5. Battery performance

As discussed above, the PMIA-based CPEs exhibited comprehensively-updated properties including mechanical strength, thermostability, ionic conductivity and interfacial stability against Li dendrites by the multifunctional PMIA additive (Table S3). To investigate their practical applications in LIBs, all-solid-state $LiFePO_4$/Li cells using the CPEs were then assembled and tested. The rate performance of the cells at 60 °C was shown in Figs. 6(a, b) and S12(A–C). The PMIA5 CPE-based cell showed much higher capacities of 151, 152, 151, 147 and 123 mAh g^{-1} than the PMIA-free cell (113, 120, 119, 111 and 63 mAh g^{-1}) at 0.1, 0.2, 0.3, 0.5 and 1.0 C, respectively (Fig. 6a). The increasing capacity with the current density from 0.1 to 0.2 C should be ascribed to the improved SPE/Li electrode interface contact and the activation of $LiFePO_4$ [36]. When the current density returned to 0.1 C again, the capacity of the PMIA5 CPE-based cell remained 152 mAh g^{-1}, which was still much higher than those of the other cells.

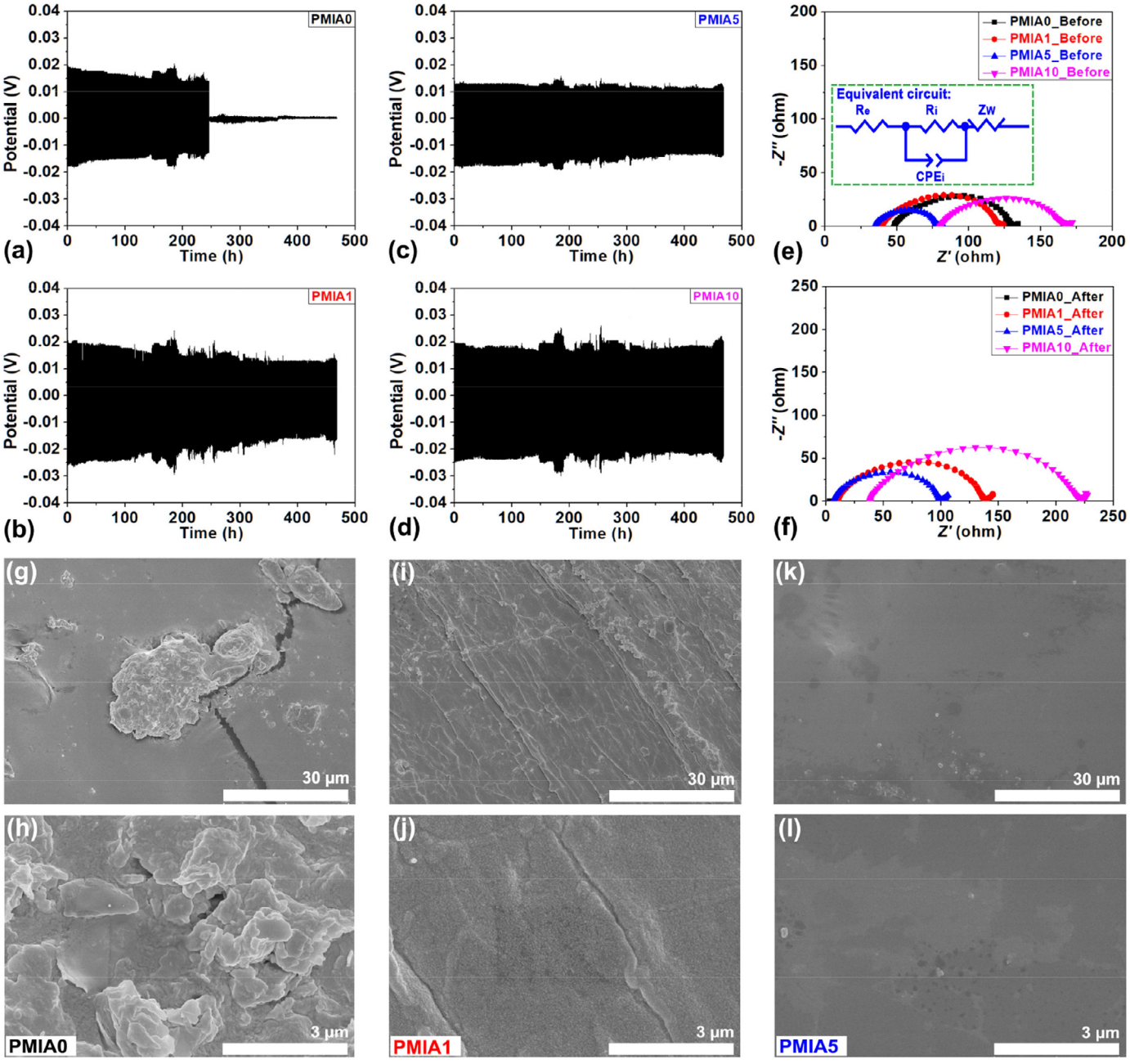

Fig. 5. Galvanostatic cycling curves of the (a) PMIA0, (b) PMIA1, (c) PMIA5, (d) PMIA10 electrolyte-based Li/Li symmetric cells under 0.10 mA cm^{-2} for 468 h at 60 °C. EIS spectra of the Li/SPE/Li cells (e) before and (f) after the Li stripping/plating processes (An equivalent circuit model is given in (e)). SEM images of the (g, h) PMIA0, (i, j) PMIA1, and (k, l) PMIA5 electrolytes after the stripping/plating processes.

The long-term cycling stability was also detected (Figs. 6c and d and S12D–F). The PMIA0-based cell showed an initial capacity of 109 mAh g^{-1}, but the capacity dropped to 75 mAh g^{-1} with capacity retention of 69% after 100 cycles at 0.5 C and 60 °C, because of the insufficient ion conductance and poor mechanical and thermal stabilities of the PMIA0 electrolyte. In comparison, the PMIA-containing cells exhibited much higher cycling stability, owing to the greatly-enhanced mechanical and thermal stabilities of the PMIA-containing CPEs. Specifically, the PMIA5 electrolyte-based cell showed the highest capacity of 137 mAh g^{-1} with capacity retention of 93% after 100 cycles. The greatly-improved battery performance should be attributed to the comprehensively-updated properties of mechanical strength, thermostability, ionic conductivity and interfacial stability against Li dendrites by the multifunctional PMIA additive (Table S3). Even compared to the all-solid-state cells with other additive-reinforced CPEs, the 5 wt% PMIA-based cells still showed superior cycling performance with respect to rate capacity and cycling stability (Table S4). Although the PMIA10 CPE-based cell had a lower initial capacity of 109 mAh g^{-1}, both the capacity of 96 mAh g^{-1} and the capacity retention of 88% after 100 cycles were higher than those of the PMIA-free cell. It should be mentioned that all the solid-state cells exhibited high Coulombic efficiencies of nearly 100% during the whole cycling (Fig. S13A). Moreover, the PMIA-containing cells had higher average discharge potentials than the PMIA-free cells during the galvanostatic cycling (Fig. S13B).

EIS measurements were further taken to investigate the impedance change (Fig. 6e and f). The semicircle in the high-

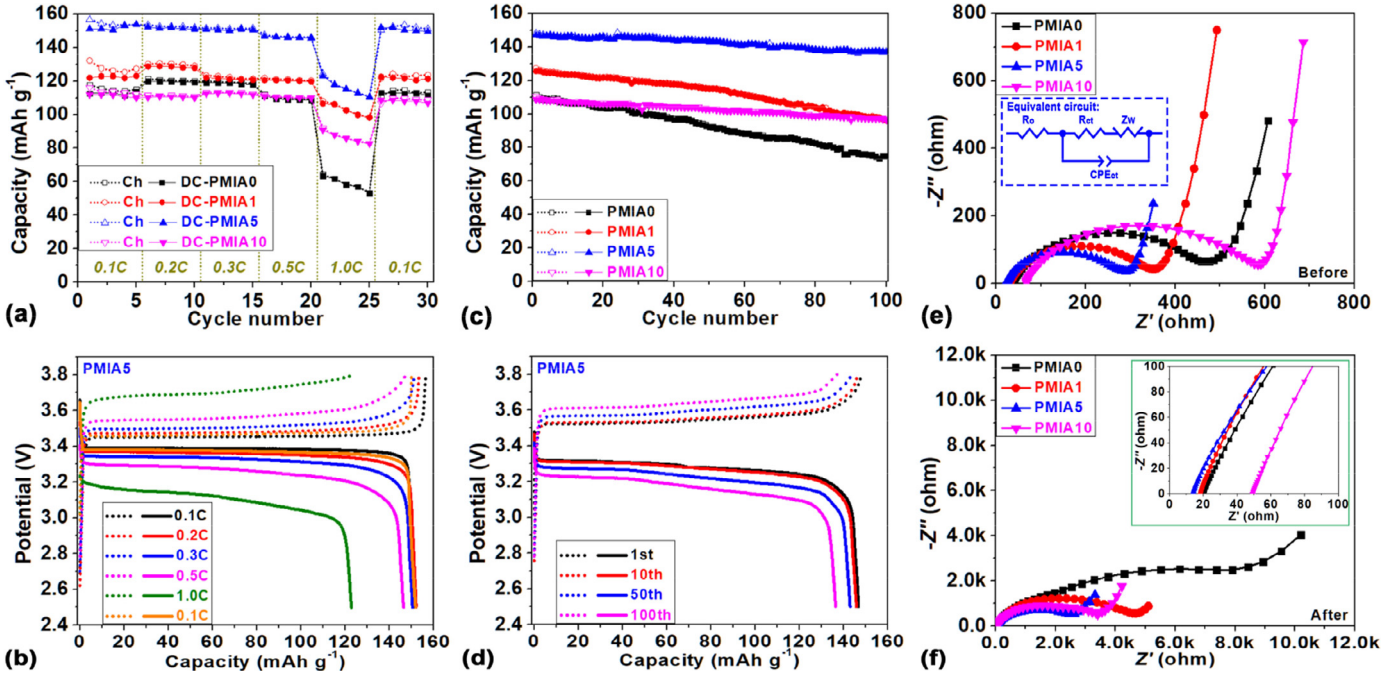

Fig. 6. (a) Rate performance of the solid-state $LiFePO_4$/Li cells at 60 °C, and (b) typical charge-discharge profiles of the PMIA5 electrolyte-based cell at various C rates. (c) Cycling performance of the solid-state cells at 0.5 C and 60 °C, and (d) charge-discharge profiles of the PMIA5 electrolyte-based cell. EIS spectra of the solid-state cells (e) before and (f) after the 100 cycles at 0.5 C and 60 °C.

frequency area and its intersection with the real axis were related to the charge transfer resistance (R_{ct}) and the ohmic resistance (R_o), respectively [28,33]. The PMIA5 CPE-based cell displayed smaller R_{ct} (267 and 2526 ohm) and R_o (23 and 14 ohm) values than the PMIA-free cell (433 and 7890 ohm for R_{ct}, and 35 and 20 ohm for R_o) both before and after the long-term cycling, reflecting the higher charge transfer in the PMIA5 CPE and again confirming the positive effect of the PMIA additive [33,36].

4. Conclusions

In summary, PMIA with abundant amide groups and high mechanical strength was employed as a multifunctional additive to prepare flexible PMIA/PEO-LiTFSI CPE membranes by simple polymer blending method. The hydrogen-bonding between PMIA and the PEO chains and $TFSI^-$ anions effectively suppressed the PEO crystallization and promoted the LiTFSI dissociation. Thus, the CPE membranes showed greatly-improved ionic conductivities (two times that of the pristine electrolyte at room temperature). With the integration of the high-strength PMIA additive with robust amide-benzene backbones, the CPE membranes also displayed greatly-enhanced mechanical tensile strength of 2.96 MPa, thermostability (419 °C) and interfacial resistance against Li dendrites (468 h at 0.10 mA cm^{-2}) than the pristine electrolyte (0.32 MPa, 364 °C, and short circuit after 246 h). The 5 wt% PMIA/PEO-LiTFSI CPE-based $LiFePO_4$/Li cells exhibited superior rate capacity (123 mAh g^{-1} at 1.0 C) and cycling stability (137 mAh g^{-1} with 93% retention after 100 cycles at 0.5 C), compared to the PMIA-free cell (63 mAh g^{-1} at 1.0 C, and 75 mAh g^{-1} with 69% retention after 100 cycles at 0.5 C). This study offers a facile and effective way to acquire comprehensively-upgraded polymer electrolytes for potential all-solid-state Li metal battery applications.

Declaration of competing interests

None.

Acknowledgments

This work is supported partially by Natural Science Foundation of Beijing Municipality (L172036), Joint Funds of the Equipment Pre-Research and Ministry of Education (6141A020225), Par-Eu Scholars Program, Science and Technology Beijing 100 Leading Talent Training Project, China Postdoctoral Science Foundation (2018M631419), Fundamental Research Funds for Central Universities (2017ZZD02, 2019QN001), and NCEPU "Double First-Class" Graduate Talent Cultivation Program.

Supplementary materials

Supplementary material associated with this article can be found, in the online version, at doi:10.1016/j.jechem.2020.02.033.

References

[1] Z. Gao, H. Sun, L. Fu, F. Ye, Y. Zhang, W. Luo, Y. Huang, Adv. Mater. 30 (2018) 1–27.
[2] H. Zhang, C. Li, M. Piszcz, E. Coya, T. Rojo, L.M. Rodriguez-Martinez, M. Armand, Z. Zhou, Chem. Soc. Rev. 46 (2017) 797–815.
[3] K. Fu, Y. Gong, J. Dai, A. Gong, X. Han, Y. Yao, C. Wang, Y. Wang, Y. Chen, C. Yan, Y. Li, E.D. Wachsman, L. Hu, Proc. Natl. Acad. Sci. USA 113 (2016) 7094–7099.
[4] J.-H. Jiang, A.-B. Wang, W.-K. Wang, Z.-Q. Jin, L.-Z. Fan, J. Energy Chem. 46 (2020) 114–122.
[5] L. Liu, M. Li, L. Chu, B. Jiang, R. Lin, X. Zhu, G. Cao, Prog. Mater. Sci. 111 (2020) 100655.
[6] X. Yao, B. Huang, J. Yin, G. Peng, Z. Huang, C. Gao, D. Liu, X. Xu, Chin. Phys. B 25 (2016) 018802.
[7] Q. Ma, H. Zhang, C. Zhou, L. Zheng, P. Cheng, J. Nie, W. Feng, Y.S. Hu, H. Li, X. Huang, L. Chen, M. Armand, Z. Zhou, Angew. Chem. Int. Ed. 55 (2016) 2521–2525.
[8] L. Chen, Y. Li, S.P. Li, L.Z. Fan, C.W. Nan, J.B. Goodenough, Nano Energy 46 (2018) 176–184.
[9] W. Liu, D. Lin, J. Sun, G. Zhou, Y. Cui, ACS Nano 10 (2016) 11407–11413.
[10] W. Liu, S.W. Lee, D. Lin, F. Shi, S. Wang, A.D. Sendek, Y. Cui, Nat. Energy 2 (2017) 1–7.
[11] C. Tao, M.H. Gao, B.H. Yin, B. Li, Y.P. Huang, G.W. Xu, J.J. Bao, Electrochim. Acta 257 (2017) 31–39.
[12] S. Gomari, M. Esfandeh, I. Ghasemi, Solid State Ionics 303 (2017) 37–46.
[13] S. Suriyakumar, S. Gopi, M. Kathiresan, S. Bose, E.B. Gowd, J.R. Nair, N. Angulakshmi, G. Meligrana, F. Bella, C. Gerbaldi, A.M. Stephan, Electrochim. Acta 285 (2018) 355–364.

[14] H. Zhai, P. Xu, M. Ning, Q. Cheng, J. Mandal, Y. Yang, Nano Lett. 17 (2017) 3182–3187.
[15] Z.J. Sun, Y.H. Li, S.Y. Zhang, L. Shi, H. Wu, H.T. Bu, S.J. Ding, J. Mater. Chem. A 7 (2019) 11069–11076.
[16] T. Watanabe, Y. Inafune, M. Tanaka, Y. Mochizuki, F. Matsumoto, H. Kawakami, J. Power Sources 423 (2019) 255–262.
[17] K.Q. He, C.L. Chen, R. Fan, C. Liu, C.Z. Liao, Y. Xu, J.N. Tang, R.K.Y. Li, Compos. Sci. Technol. 175 (2019) 28–34.
[18] Q. Lu, J. Fang, J. Yang, G. Yan, S. Liu, J. Wang, J. Membr. Sci. 425-426 (2013) 105–112.
[19] L. Liu, M. Li, L. Chu, B. Jiang, R. Lin, Appl. Surf. Sci. 476 (2019) 501–512.
[20] G. Luo, B. Yuan, T. Guan, F. Cheng, W. Zhang, J. Chen, ACS Appl. Energy Mater. 2 (2019) 3028–3034.
[21] G. Zhu, X. Jing, D. Chen, W. He, Int. J. Hydrogen Energy 45 (2020) 2917–2924.
[22] Y. Zhang, W. Lu, L. Cong, J. Liu, L. Sun, A. Mauger, C.M. Julien, H. Xie, J. Liu, J. Power Sources 420 (2019) 63–72.
[23] L. Liu, J. Lyu, J. Mo, P. Peng, J. Li, B. Jiang, L. Chu, M. Li, Sci. China Mater. (2020) press, doi:10.1007/s40843-019-1240-2.
[24] X.F. Yang, Q. Sun, C.T. Zhao, X.J. Gao, K.R. Adair, Y.L. Liu, J. Luo, X.T. Lin, J.N. Liang, H. Huang, L. Zhang, R. Yang, S.G. Lu, R.Y. Li, X.L. Sun, Nano Energy 61 (2019) 567–575.
[25] H. Duan, Y.-X. Yin, X.-X. Zeng, J.-Y. Li, J.-L. Shi, Y. Shi, R. Wen, Y.-G. Guo, L.-J. Wan, Energy Storage Mater. 10 (2018) 85–91.
[26] Z.-J. He, L.-Z. Fan, Rare Met. 37 (2018) 488–496.
[27] W. Liu, N. Liu, J. Sun, P.C. Hsu, Y. Li, H.W. Lee, Y. Cui, Nano Lett. 15 (2015) 2740–2745.
[28] J. Zhang, X. Zang, H. Wen, T. Dong, J. Chai, Y. Li, B. Chen, J. Zhao, S. Dong, J. Ma, L. Yue, Z. Liu, X. Guo, G. Cui, L. Chen, J. Mater. Chem. A 5 (2017) 4940–4948.
[29] X. Fu, C. Li, Y. Wang, L.P. Kovatch, L. Scudiero, J. Liu, W. Zhong, ACS Appl. Mater. Interfaces 10 (2018) 4726–4736.
[30] J. Hu, W.H. Wang, B.H. Zhou, Y.Z. Feng, X.L. Xie, Z.G. Xue, J. Membr. Sci. 575 (2019) 200–208.
[31] S.-J. Tan, X.-X. Zeng, Q. Ma, X.-W. Wu, Y.-G. Guo, Electrochem. Energy Rev. 1 (2018) 113–138.
[32] W. Li, S. Zhang, B. Wang, S. Gu, D. Xu, J. Wang, C. Chen, Z. Wen, ACS Appl. Mater. Interfaces 10 (2018) 23874–23882.
[33] O. Sheng, C. Jin, J. Luo, H. Yuan, H. Huang, Y. Gan, J. Zhang, Y. Xia, C. Liang, W. Zhang, X. Tao, Nano Lett. 18 (2018) 3104–3112.
[34] D. Lin, W. Liu, Y. Liu, H.R. Lee, P.C. Hsu, K. Liu, Y. Cui, Nano Lett. 16 (2016) 459–465.
[35] M. Dirican, C.Y. Yan, P. Zhu, X.W. Zhang, Mater. Sci. Eng. R 136 (2019) 27–46.
[36] L. Liu, L. Chu, B. Jiang, M. Li, Solid State Ionics 331 (2019) 89–95.
[37] S. Chen, J. Wang, Z. Zhang, L. Wu, L. Yao, Z. Wei, Y. Deng, D. Xie, X. Yao, X. Xu, J. Power Sources 387 (2018) 72–80.
[38] J. Bae, Y. Li, J. Zhang, X. Zhou, F. Zhao, Y. Shi, J.B. Goodenough, G. Yu, Angew. Chem. Int. Ed. 57 (2018) 2096–2100.
[39] D. Lin, P.Y. Yuen, Y. Liu, W. Liu, N. Liu, R.H. Dauskardt, Y. Cui, Adv. Mater. 30 (2018) 1802661.
[40] P. Zhu, C. Yan, M. Dirican, J. Zhu, J. Zang, R.K. Selvan, C.-C. Chung, H. Jia, Y. Li, Y. Kiyak, N. Wu, X. Zhang, J. Mater. Chem. A 6 (2018) 4279–4285.
[41] L. Zhu, P. Zhu, Q. Fang, M. Jing, X. Shen, L. Yang, Electrochim. Acta 292 (2018) 718–726.
[42] A.M. Rocco, C.P. da Fonseca, R.P. Pereira, Polymer 43 (2002) 3601–3609.
[43] J.J. Bao, X.B. Qu, G.Q. Qi, Q.K. Huang, S.F. Wu, C. Tao, M.H. Gao, C.H. Chen, Solid State Ionics 320 (2018) 55–63.
[44] Y.-J. Li, C.-Y. Fan, J.-P. Zhang, X.-L. Wu, Dalton Trans. 47 (2018) 14932–14937.
[45] Y.F. Liang, Y. Xia, S.Z. Zhang, X.L. Wang, X.H. Xia, C.D. Gu, J.B. Wu, J.P. Tu, Electrochim. Acta 296 (2019) 1064–1069.
[46] X.-Y. Yu, M. Xiao, S.-J. Wang, Q.-Q. Zhao, Y.-Z. Meng, J. Appl. Polym. Sci. 115 (2010) 2718–2722.
[47] A.M. Rocco, R.P. Pereira, Solid State Ionics 279 (2015) 78–89.
[48] Y. Lim, H.-A. Jung, H. Hwang, Energies 11 (2018) 2559.
[49] J. B, A. Km, M. M, P. V.S, J. S, Electrochim. Acta 235 (2017) 210–222.
[50] E. Glynos, P. Petropoulou, E. Mygiakis, A.D. Nega, W. Pan, L. Papoutsakis, E.P. Giannelis, G. Sakellariou, S.H. Anastasiadis, Macromolecules 51 (2018) 2542–2550.
[51] A.B. Puthirath, S. Patra, S. Pal, M. M, A. Puthirath Balan, J. S, N. Tharangattu N, J. Mater. Chem. A 5 (2017) 11152–11162.
[52] T. Wang, R. Zhang, Y. Wu, G. Zhu, C. Hu, J. Wen, W. Luo, J. Energy Chem. 46 (2020) 187–190.
[53] M. Yang, C. Zhao, S. Zhang, P. Li, D. Hou, Appl. Surf. Sci. 394 (2017) 149–159.
[54] C.E. Lin, J. Wang, M.Y. Zhou, B.K. Zhu, L.P. Zhu, C.J. Gao, J. Membr. Sci. 518 (2016) 72–78.
[55] H. Zhang, Y. Zhang, T. Xu, A.E. John, Y. Li, W. Li, B. Zhu, J. Power Sources 329 (2016) 8–16.
[56] S.-O. Tung, S. Ho, M. Yang, R. Zhang, N.A. Kotov, Nat. Commun. 6 (2015) 6152.
[57] S. Hu, S. Lin, Y. Tu, J. Hu, Y. Wu, G. Liu, F. Li, F. Yu, T. Jiang, J. Mater. Chem. A 4 (2016) 3513–3526.
[58] X. Zhang, N. Li, Z. Hu, J. Yu, Y. Wang, J. Zhu, J. Membr. Sci. 581 (2019) 355–361.
[59] L. Yao, C. Lee, J. Kim, Fiber Polym. 11 (2010) 1032–1040.
[60] X. Zhang, J. Xie, F. Shi, D. Lin, Y. Liu, W. Liu, A. Pei, Y. Gong, H. Wang, K. Liu, Y. Xiang, Y. Cui, Nano Lett. 18 (2018) 3829–3838.
[61] X. Wang, Y. Zhang, X. Zhang, T. Liu, Y.-H. Lin, L. Li, Y. Shen, C.-W. Nan, ACS Appl. Mater. Interfaces 10 (2018) 24791–24798.
[62] W. Li, S. Zhang, B. Wang, S. Gu, D. Xu, J. Wang, C. Chen, Z. Wen, ACS Appl. Mater. Interfaces 10 (2018) 23874–23882.
[63] S. Das, A. Ghosh, J. Phys. Chem. B 121 (2017) 5422–5432.
[64] J. B, A. Km, M. M, P. V.S, J. S, Electrochim. Acta 235 (2017) 210–222.
[65] P.P. Chu, M.J. Reddy, H.M. Kao, Solid State Ionics 156 (2003) 141–153.
[66] Q. Zhou, J. Ma, S. Dong, X. Li, G. Cui, Adv. Mater. (2019) 1902029.
[67] Q. Zhang, K. Liu, F. Ding, X. Liu, Nano Res. 10 (2017) 4139–4174.
[68] L. Liu, J. Lyu, J. Mo, H. Yan, L. Xu, P. Peng, J. Li, B. Jiang, L. Chu, M. Li, Nano Energy 69 (2020) 104398.
[69] K. Vignarooban, M.A.K.L. Dissanayake, I. Albinsson, B.E. Mellander, Solid State Ionics 266 (2014) 25–28.
[70] X.-B. Fu, L.-Y. Yang, J.-Q. Ma, G. Yang, Y.-F. Yao, Q. Chen, Polymer 105 (2016) 310–317.
[71] E. Kharlampieva, V. Kozlovskaya, S.A. Sukhishvili, Adv. Mater. 21 (2009) 3053–3065.
[72] R. Khurana, J.L. Schaefer, L.A. Archer, G.W. Coates, J. Am. Chem. Soc. 136 (2014) 7395–7402.
[73] M. Yang, K. Cao, B. Yeom, M.D. Thouless, A. Waas, E.M. Arruda, N.A. Kotov, J. Compos. Mater. 49 (2015) 1873–1879.
[74] F. Lu, C. Zhang, B. Lu, K. Yu, J. Liu, H. Kang, R. Liu, G. Lan, Cellulose 24 (2017) 1621–1629.
[75] A. Blazejczyk, W. Wieczorek, R. Kovarsky, D. Golodnitsky, E. Peled, L.G. Scanlon, G.B. Appetecchi, B. Scrosati, J. Electrochem. Soc. 151 (2004) A1762–A1766.
[76] A. Blazejczyk, M. Szczupak, W. Wieczorek, P. Cmoch, G.B. Appetecchi, B. Scrosati, R. Kovarsky, D. Golodnitsky, E. Peled, Chem. Mater. 17 (2005) 1535–1547.
[77] A.M. Stephan, T.P. Kumar, N. Angulakshmi, P.S. Salini, R. Sabarinathan, A. Srinivasan, S. Thomas, J. Appl. Polym. Sci. 120 (2011) 2215–2221.
[78] K. Karthik, R. Murugan, J. Solid State Electrochem. 22 (2018) 2989–2998.
[79] M. Sasikumar, M. Raja, R.H. Krishna, A. Jagadeesan, P. Sivakumar, S. Rajendran, J. Phys. Chem. C 122 (2018) 25741–25752.
[80] A.S. Pandian, X.C. Chen, J. Chen, B.S. Lokitz, R.E. Ruther, G. Yang, K. Lou, J. Nanda, F.M. Delnick, N.J. Dudney, J. Power Sources 390 (2018) 153–164.
[81] W. Tang, S. Tang, C. Zhang, Q. Ma, Q. Xiang, Y.-W. Yang, J. Luo, Adv. Energy Mater. 8 (2018) 1800866.
[82] B. Yuan, G. Luo, J. Liang, F. Cheng, W. Zhang, J. Chen, J. Energy Chem. 38 (2019) 55–59.
[83] S. Liu, H. Wang, N. Imanishi, T. Zhang, A. Hirano, Y. Takeda, O. Yamamoto, J. Yang, J. Power Sources 196 (2011) 7681–7686.
[84] X. Li, D. Wang, H. Wang, H. Yan, Z. Gong, Y. Yang, ACS Appl. Mater. Interfaces 11 (2019) 22745–22753.
[85] T. Watanabe, Y. Inafune, M. Tanaka, Y. Mochizuki, F. Matsumoto, H. Kawakami, J. Power Sources 423 (2019) 255–262.
[86] J. Lyu, Z. Liu, X. Wu, G. Li, D. Fang, X. Zhang, ACS Nano 13 (2019) 2236–2245.
[87] L. Chen, W. Li, L.-Z. Fan, C.-W. Nan, Q. Zhang, Adv. Funct. Mater. 29 (2019) 1901047.
[88] T. Yang, J. Zheng, Q. Cheng, Y.-Y. Hu, C.K. Chan, ACS Appl. Mater. Interfaces 9 (2017) 21773–21780.
[89] L. Liu, B.G. Choi, S.O. Tung, J. Lyu, T. Li, T. Zhao, N.A. Kotov, J. Phys. Chem. C 122 (2018) 14014–14028.
[90] C. Xiong, Q. Yang, W. Dang, M. Li, B. Li, J. Su, Y. Liu, W. Zhao, C. Duan, L. Dai, Y. Xu, Y. Ni, J. Power Sources 447 (2020) 227387.
[91] L. Chen, L.Z. Fan, Energy Storage Mater. 15 (2018) 37–45.
[92] X. Fan, X. Ji, F. Han, J. Yue, J. Chen, L. Chen, T. Deng, J. Jiang, C. Wang, Sci. Adv. 4 (2018) eaau9245.